scientific reports

Check for updates

OPEN

Highly efficient visible light active iron oxide-based photocatalysts for both hydrogen production and dye degradation

Preethi Vijayarengan[1,2]✉, Sri Chandana Panchangam[3]✉, Ananth Stephen[4], Gokulanandhan Bernatsha[1], Gokul Krishnan Murali[1], Subramanyam Sarma Loka[5], Sathish Kumar Manoharan[6], Venkatramu Vemula[7], Rama Rao Karri[8]✉ & Gobinath Ravindran[9]

Photocatalysis is essential for wastewater cleanup and clean energy, and in this current study, we have synthesized nanomaterials (iron oxide-based) for photocatalytic pollution degradation and hydrogen production. The performance of aluminium oxide/ferric oxide (Al_2O_3/Fe_2O_3), samarium oxide/ferric oxide (Sm_2O_3/Fe_2O_3) and yttrium oxide/ferric oxide (Y_2O_3/Fe_2O_3) were compared for the production of hydrogen (H_2) and degradation of dye under natural sunlight. Various characterisation equipment was used to characterize these photocatalysts' structure, morphology, elemental content, binding energy and band gap. The hydrogen recovery efficiency of iron oxide-based photocatalysts from sulphide-containing wastewater is assessed. Y_2O_3/Fe_2O_3 has shown the highest hydrogen production of 340 mL/h. The influence of operating factors such as sulphide ion concentration, catalyst quantity, and photocatalyst photolytic solution volume on hydrogen production is studied. The optimal values were 0.25 M, 0.2 g/L, and 1L, respectively. The developed photocatalyst passed multiple cycles of stability testing. Fe_2O_3 has shown the highest Rhodamine B (RhB) dye degradation efficiency of 94% under visible light.

Keywords H_2 production, Yttrium oxide, Ferric oxide, RhB, Degradation

Accelerated technological advancements and strong economic growth have increased global energy demand, highlighting the critical need for energy conservation and efficiency. The replenishment of scarce and rapidly depleting fossil fuels takes ages and cannot meet the escalating rate of energy demand. With rapid industrialization and expanding urbanization, there has been greater emphasis on the need for comprehensive research studies on energy consumption, its impact on the environment and the use of renewable energy for promoting sustainability[1,2]. Earlier research has shown that the photocatalytic process under visible light could be used for the effective generation of renewable energy (H_2 evolution) and in the degradation of toxic wastewater pollutants[3]. Many research studies have focussed on exploring photocatalytic materials that are active under visible light and stable during the photocatalytic process, thus achieving maximum hydrogen production and complete mineralization of pollutants. Clean renewable energy production from cheap resources like wastewater is the need of the hour for energy security. At the same time, removing harmful contaminants from wastewater is a challenging problem that must be tackled to protect and preserve the environment. Organic dyes are used in several applications, such as cosmetics, textiles, paper industry, and other colourants, and they eventually enter into water bodies. These dyes are pollutants that must be treated effectively to achieve maximum removal

[1]Department of Civil Engineering, Hindustan Institute of Technology and Science, Chennai 603103, India. [2]Department of Civil Engineering, Sri Sivasubramaniya Nadar College of Engineering, Chennai 603110, India. [3]Department of Civil Engineering, Annamacharya Institute of Technology and Sciences, Kadapa 516003, India. [4]Department of Physics, KPR Institute of Engineering and Technology, Coimbatore 641407, India. [5]Nanoelectrochemistry Laboratory, Department of Chemistry, Yogi Vemana University, Kadapa 516003, India. [6]Department of Biotechnology, Anand Institute of Higher Technology, OMR, Kazhipattur, Chennai 603103, India. [7]Department of Physics, Yogi Vemana University, Kadapa 516 005, India. [8]Petroleum and Chemical Engineering, Faculty of Engineering, Universiti Teknologi Brunei, Bandar Seri Begawan BE1410, Brunei Darussalam. [9]Department of Civil Engineering, SR University, Warangal, Telangana 506371, India. ✉email: preethi_enviro@hotmail.com; srichandanaloka@gmail.com; kramarao.iitd@gmail.com

efficiency[4]. Photocatalytic removal of the organic dyes from the environmental water matrix offers the following advantages, i.e., (a) utilization of renewable solar energy and (b) cost-effective pollution mitigation[5]. The photocatalytic process is an efficient method that can be employed for the twin uses of removal of wastewater pollutants and hydrogen production[6–8]. The adopted method offers noteworthy economic and environmental benefits. Photocatalytic degradation or H_2 production is considered suitable because of its economical, eco-friendly, and convenient nature. The photocatalytic reaction requires a potential of 1.23 eV per electron to obtain desirable H_2, O_2 and CO_2 molecules and comprises three significant steps: electron and hole pairs generation, charge isolation and migration to the catalyst surface, and chemical reaction on the active sites[9].

Fe_2O_3 is a potential photocatalyst with a narrow band gap (< 2.1 eV) and a vast absorption capacity in the visible light area. The photocatalytic activity of Fe_2O_3 increases in a concurrent system during real-time applications. Interfacing of other metal oxides with Fe_2O_3 will likely result in substantial improvement in the photocatalytic efficacy. Iron oxide facilitates the sinking of photogenerated electrons and hole pairs in a co-catalyst lattice, thereby increasing the charge separation and improving the corresponding photoactivity[10]. Furthermore, there are a more significant number of active sites in a co-catalyst system when compared to a pristine catalyst. Maximum active sites are at the disposal of a co-catalyst system when compared to a pristine catalyst. The increased number of available active sites aids in enhanced hydrogen production and improved dye degradation[11–13]. Most research studies have combined iron oxide with titania-based photocatalysts or other semiconductors[10,14]. The application of nanocomposite metal oxide materials as a photocatalyst to remove wastewater contaminants was examined, and it resulted in better photocatalytic activity than the oxides alone. Composite nanostructured metal oxides are an interesting option against doping techniques. The nanocomposites enhanced the properties of the metal oxides[15]. Few research papers have reported visible, active photocatalytic dye degradation[16].

The current research study discusses the photocatalytic efficiency of visible-light-induced iron oxide composites like Al_2O_3/Fe_2O_3, Sm_2O_3/Fe_2O_3, and Y_2O_3/Fe_2O_3 to recover hydrogen from sulphide-containing wastewater and degrade the organic pollutant, Rhodamine B (RhB) dye. These iron oxide composites are synthesized in a novel route and have not yet been reported by other researchers. The photocatalysts are well characterized, and the factors affecting photocatalytic reactions of H_2 production and dye degradation are studied.

Materials, synthesis and characterization of iron-oxide-based photocatalysts

Iron oxide nanoparticles are synthesised by the combustion process, using cow urine as the natural urea source. Cow urine is obtained from nearby farmers. Analytical grade Rhodamine B (RhB) is procured from M/s S.D. Fine Chemicals, Mumbai, India. Ferric nitrate, urea, aluminium nitrate, yttrium nitrate, and samarium nitrate are obtained from Merck Chemicals, India, and have a purity of 99.99%.

Synthesis of pure iron oxide

At first, 40.4 g of ferric nitrate ($Fe(NO_3)_3{\cdot}9H_2O$) is dissolved in 100 mL natural urea solution and stirred for 30 min to obtain a homogeneous mixture. Later, this homogeneous solution is heated continuously on a hot plate. Upon heating for an hour, this homogeneous mixture of urea-iron nitrate solution turns into a transparent viscous gel that auto-ignites to form voluminous foam. Further continual heating transforms the foam into dry nanoparticles because of combustion. A schematic representation of the preparation of iron oxide nanoparticles is provided in Fig. 1.

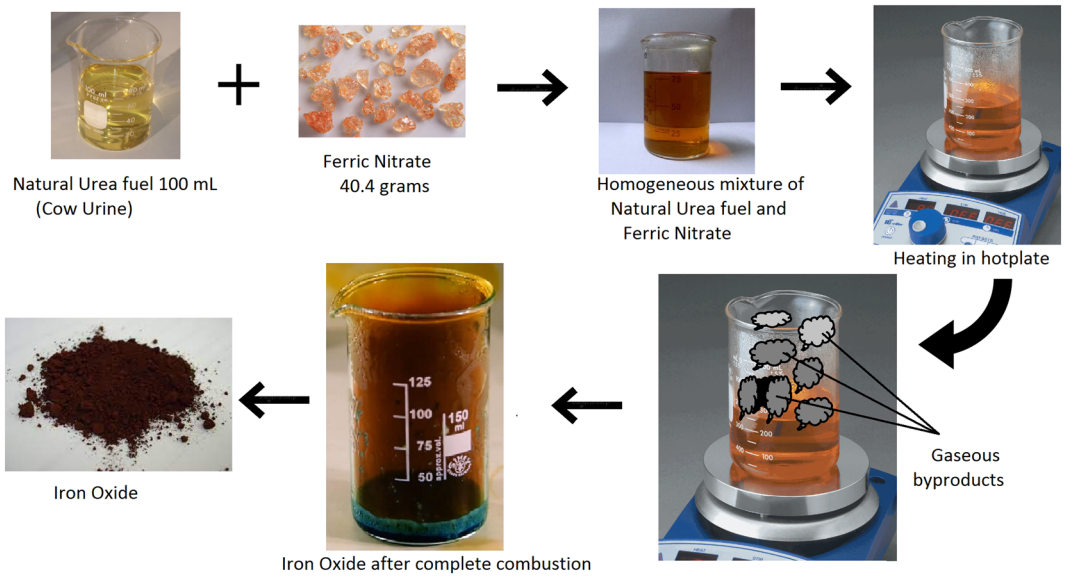

Figure 1. Synthesis of iron oxide nanoparticles.

Synthesis of aluminium oxide: iron oxide

A similar combustion process, as described above using natural urea fuel, is adopted to synthesise aluminium oxide: iron oxide nanoparticles. An equimolar ratio of ferric nitrate and aluminium nitrate ($Al(NO_3)_3 \cdot 9H_2O$) is taken and dissolved individually in a 50 mL quantity of fuel. After ensuring complete solubility, both solutions are transferred into a single container and thoroughly mixed to form a homogeneous solution. Then, this homogeneous mixture is heated on a hot plate to facilitate the combustion process. Figure 2 depicts the synthesis procedure of Al_2O_3/Fe_2O_3 nanoparticles.

Synthesis of yttrium oxide: iron oxide and samarium oxide: iron oxide

For the Yttrium oxide: iron oxide (Y_2O_3/Fe_2O_3) synthesis, ferric nitrate, and Yttrium nitrate ($Y(NO_3)_3.6H_2O$) are taken as precursor materials in equimolar ratio and dissolved individually in 50 ml natural urea. Similarly, for the samarium oxide: iron oxide (Sm_2O_3/Fe_2O_3) synthesis process, ferric nitrate and Samarium nitrate ($Sm(NO_3)_3 \cdot 6H_2O$) are taken as the precursor materials. The preparation of the homogeneous mixture and combustion process is the same as explained in the earlier section. All the processes yield ultra-fine particles, which are dried and powdered well for further studies and characterization.

Characterization of photocatalysts

The prepared photocatalysts are thoroughly characterized with X-ray diffraction measurements of Fe_2O_3 and other mixed metal oxides using a Rigaku Miniflex-600 X-ray diffractometer operated with Cu Kα radiation ($\lambda = 1.54$ Å) in the 2θ range of 0° to 90°. Morphological features of Fe_2O_3 and other mixed metal oxides are obtained using Scanning Electron Microscopy (SEM). A JEOL JSM-IT 500 scanning electron microscope is operated at 25 kV. For SEM analysis, the powder samples are glued to carbon adhesive tape. Energy dispersive X-ray (EDX) analysis is done to identify metals and oxygen species with a built-in dry silicon-drift EDX detector integrated with the SEM instrument. UV–vis Diffuse Reflectance spectrum (UV-DRS) obtained with a JASCO V755 UV–vis spectrophotometer is used to determine the photocatalysts' band structure and light-absorbing capacity.

Photocatalytic experiments for H_2 production and dye degradation

A photocatalytic reactor of five-litre capacity is used for hydrogen recovery. The reactor is made of acrylic material with a trapezoidal shape. Simulated sulphide wastewater consisting of sulphide ion concentrations in the range of 0.05 M to 0.3 M, with 0.2 M in a typical system, is used for hydrogen recovery. Sulphide ion acts as the sacrificial agent in the hydrogen production process. Different doses of iron oxide-based photocatalysts are employed. The hydrogen produced during the process is collected in an inverted measuring cylinder. All the experiments are conducted from 12 to 2 PM when the sunlight intensity is at its peak.

A 50 mg/L stock solution of RhB is prepared, and the necessary dilutions are made from the stock solution. RhB is quantified by a UV–Vis double beam Spectrophotometer (Systronics Model No. 2203) with a wavelength range of 200 to 1100 nm with an accuracy of 0.5 nm and a bandwidth of 2 nm. The photometric range of absorbance for the instrument is ± 2.5 ABS. The peak absorbance wavelength of RhB used in the study is 554.8 nm. A calibration graph for RhB quantification with concentrations 0–25 mg/L is prepared. The linear fitting is achieved with a coefficient of determination (R^2) value of 0.999. The concentration of RhB in the unknown sample is determined using this calibration graph.

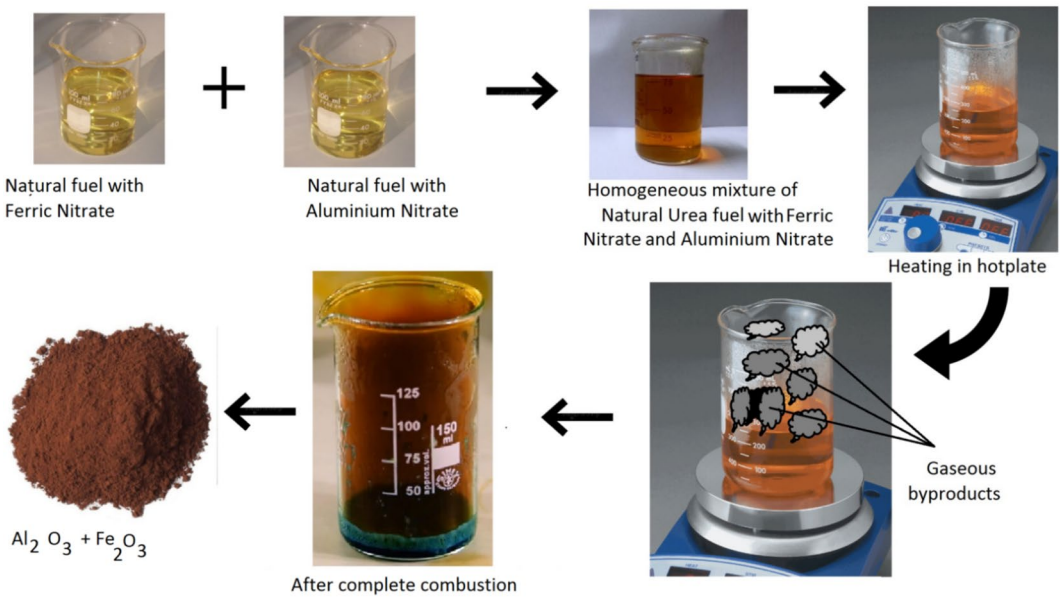

Figure 2. Synthesis of Al_2O_3/Fe_2O_3 nanoparticles.

Photocatalytic degradation of RhB is carried out in a 1 L volume double-jacketed quartz reactor with an inlet and outlet. A 125 W Vis Lamp with a built-in safety resister is used as a light source to provide illumination. The lamp is placed in the quartz sleeve and is in the provision given in the reactor vessel. An initial RhB concentration of 5 mg/L is used in a typical experiment while the catalyst dose is maintained at 200 mg/L. All the reaction solutions are stirred in the dark for half an hour before they are exposed to visible light illumination to attain adsorption–desorption equilibrium between the photocatalysts and the RhB dye. The solution is illuminated for 4 h, and the samples are withdrawn every 15 min to determine RhB concentration. The solution is continuously stirred at 600 rpm using a magnetic stirrer while the temperature is maintained at 25 ± 2 °C using a cooling tank with a pump. The pH of the samples was not controlled during the experiments; however, the initial pH was within the range of 6.5 to 9 during the entire experiment. The collected samples are centrifuged at 5000 rpm with Remi make model number R-24 centrifuge. The supernatant from the centrifuge tube is collected in vials for the RhB quantification.

Results and discussions

Characterization of photocatalysts

Figure 3 shows the XRD patterns of Fe_2O_3 and other mixed metal oxides. In the case of the XRD scan of Fe_2O_3, well-defined peaks appear at 26.67°, 33.21°, 35.98°, 42.58° and they are compared with standard XRD for the hematite phase of Fe_2O_3 (JCPDS card number 39-1346). Further, sharp and strong peaks are observed for Fe_2O_3, revealing that the prepared metal oxide is crystalline. No peaks related to the Fe_2O_3 phase are observed in the XRD scan of Al_2O_3/Fe_2O_3. Close inspection of the XRD scan reveals a broad peak between 2θ between 25° and 30° originating from the diffraction of the (220) plane of γ-Al_2O_3[17].

Further, coverage of iron oxide by aluminium oxide particles may have contributed to the absence of XRD peaks related to the iron oxide. In the case of other mixed metal oxides like Sm_2O_3/Fe_2O_3 and Y_2O_3/Fe_2O_3, observed peaks comprise of contribution from both the metal oxides. From the XRD analysis, it is evident that except Al_2O_3/Fe_2O_3, other mixed metal oxides are reasonably crystalline in nature, and hence better photocatalytic activity can be anticipated.

The morphological features observed for Fe_2O_3 and other mixed metal oxides are examined using scanning electron microscopy (SEM) and are presented in Fig. 4. It is seen that the Fe_2O_3 particles have a plate-like morphology and are porous in nature. In the case of mixed Al_2O_3/Fe_2O_3, it can be seen that some numbers of spherical aggregates are deposited on Fe_2O_3. Similar observations can be seen for other mixed metal oxides like Sm_2O_3/Fe_2O_3 and Y_2O_3/Fe_2O_3. Fe and other metal components in mixed metal oxides are verified from energy dispersive X-ray analysis (EDX) (Fig. SI 1: Supplementary Information).

The optical absorption potential of the photocatalysts is assessed using UV-DRS spectrum recorded within the 200 nm to 800 nm range, as shown in Fig. 5a. All the iron oxide-based photocatalysts exhibit high visible photoactivity with a typical absorption broad peak at around 400–500 nm. The absorbance of photocatalysts is

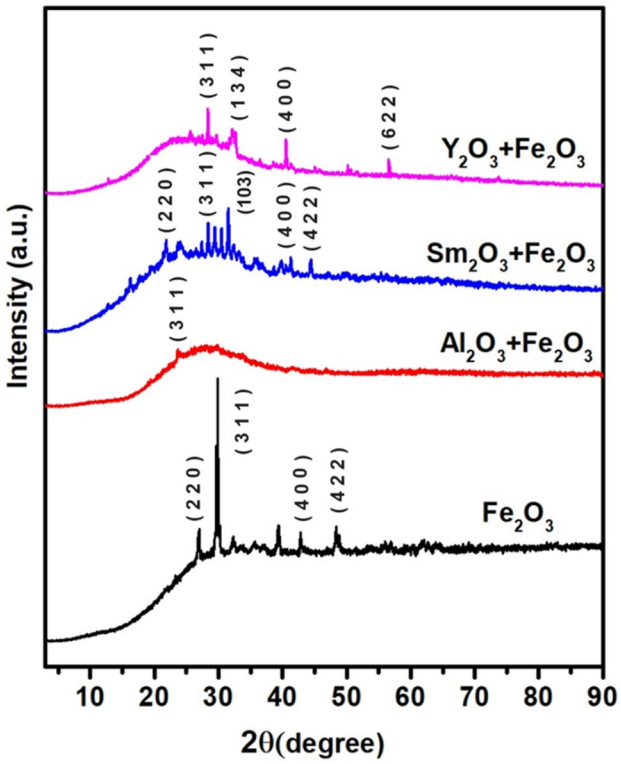

Figure 3. X-ray diffraction patterns of Fe_2O_3, Al_2O_3/Fe_2O_3, Sm_2O_3/Fe_2O_3, and Y_2O_3/Fe_2O_3.

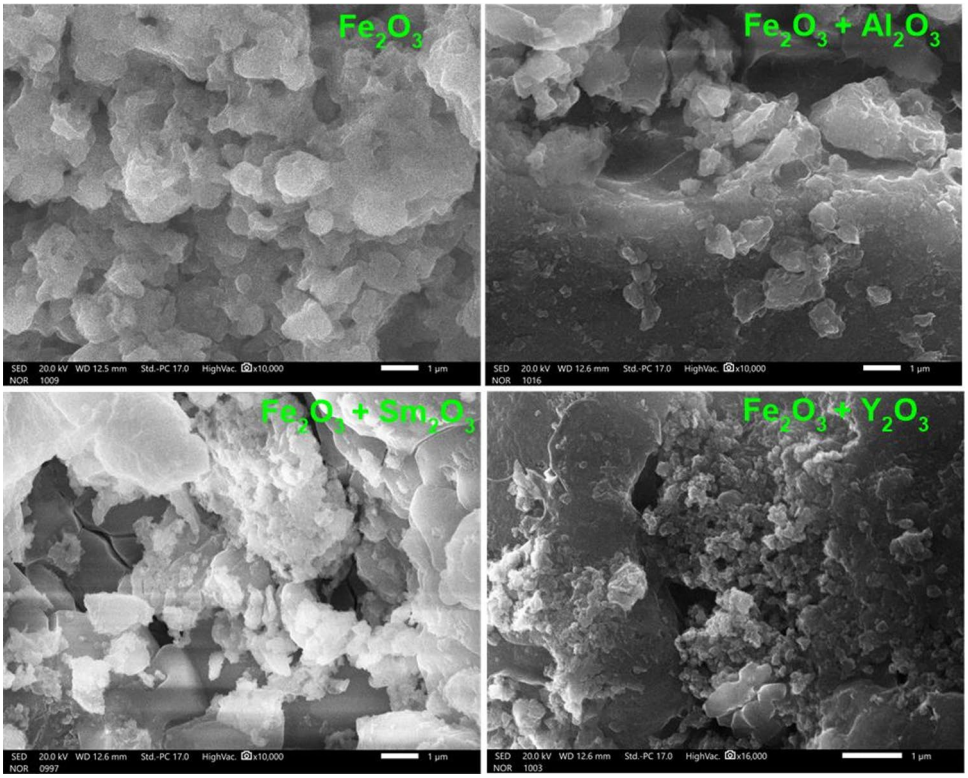

Figure 4. Scanning electron microscopy (SEM) images of Fe_2O_3, Al_2O_3/Fe_2O_3, Sm_2O_3/Fe_2O_3, and Y_2O_3/Fe_2O_3.

in the following order: $Al_2O_3/Fe_2O_3 > Sm_2O_3/Fe_2O_3 > Y_2O3/Fe_2O_3$. The bandgap of the iron oxide-based photocatalysts is determined using Kubelka–Munk plots, as shown in Fig. 5b. The band gap values of the photocatalysts are 1.5, 1.6, 1.9, and 1.7 for Fe_2O_3, Al_2O_3/Fe_2O_3, Sm_2O_3/Fe_2O_3 and Y_2O_3/Fe_2O_3, respectively.

The chemical state, valency, binding energy, etc., can be obtained from XPS analysis. The optical application is based on the valence state of the synthesized iron oxide-based NPs. Figure 6 shows the valence band XPS spectra of Fe_2O_3, Al_2O_3/Fe_2O_3, Y_2O_3/Fe_2O_3 and Sm_2O_3/Fe_2O_3. The presence of Fe^{2+} is well bonded with the Al and O in Al_2O_3/Fe_2O_3 sample. Hence, the iron is more sensitive than aluminium for the oxidation process. The metal ions are surface bonded with lattice oxygen. The obtained valency state has opted for the photocatalytic application. The binding energy of 2p3/2 and 2p1/2 states located at 711 and 714 eV agree with the standard values and confirm the configuration of Fe_2O_3. The binding energy of the other elements matches the XPS spectral data. The binding energies are slightly altered and raised in doped Fe_2O_3 owing to the inclusion of Al_2O_3, Y_2O_3 and Sm_2O_3. The results obtained demonstrate the high purity of Al_2O_3/Fe_2O_3 NPs. The oxidized metal NPs are widely employed for catalytic applications.

Photocatalytic solar hydrogen production

Simulated sulphide wastewater with 0.2 M sulphide ion concentration is used for the H_2 production study. The efficiencies of various iron oxide (Fe_2O_3) photocatalysts are determined to determine their photocatalytic activity. In a typical reactor, as soon as the Fe_2O_3-based photocatalysts are exposed to solar irradiation, electrons are generated, and holes are produced, leading to reduction and oxidation reactions, respectively, to form hydrogen. The solar light intensity is determined with the help of a lux meter and is seen to vary from 75,000 to 82,000 lx. Figure 7a shows the photographic view of the photocatalytic reactor utilized for hydrogen production, and Fig. 7b depicts the activity of various iron oxide-based photocatalysts used for hydrogen production. Regarding hydrogen production efficiency, Y_2O_3/Fe_2O_3 are observed to have maximum efficiency with 340 mL of H_2 per hour. There is a reduction in the H_2 production efficiency in the following order: Y_2O_3/Fe_2O_3 (340 mL/h) > Al_2O_3/Fe_2O_3 (250 mL/h) > Sm_2O_3/Fe_2O_3 (200 mL/h) > Fe_2O_3 (135 mL/h). The Y_2O_3 increases the H_2 production efficiency by 2.5 times compared to pure Fe_2O_3. Y_2O_3 is one of the heavy rare earth oxides with a small atomic radius, which helps accelerate the photoactivity of the attached co-catalyst[18].

Sacrificial agent

Synthetic wastewater with 0.2 M sulphide concentration and 0.1 g of Y_2O_3/ Fe_2O_3 is used to estimate the effect of sulphite ion concentrations as a sacrificial agent for maximum hydrogen production. The sulphite ion concentrations are varied from 0.05 to 0.3 M with an interval of 0.05 M. The optimized sulphide ion concentration will help to suppress photo-corrosion[19]. Figure 8 depicts the effects of sulphite ion concentrations on hydrogen recovery. The generation of H_2 was found to decrease with an increase in sulphite ion concentration beyond

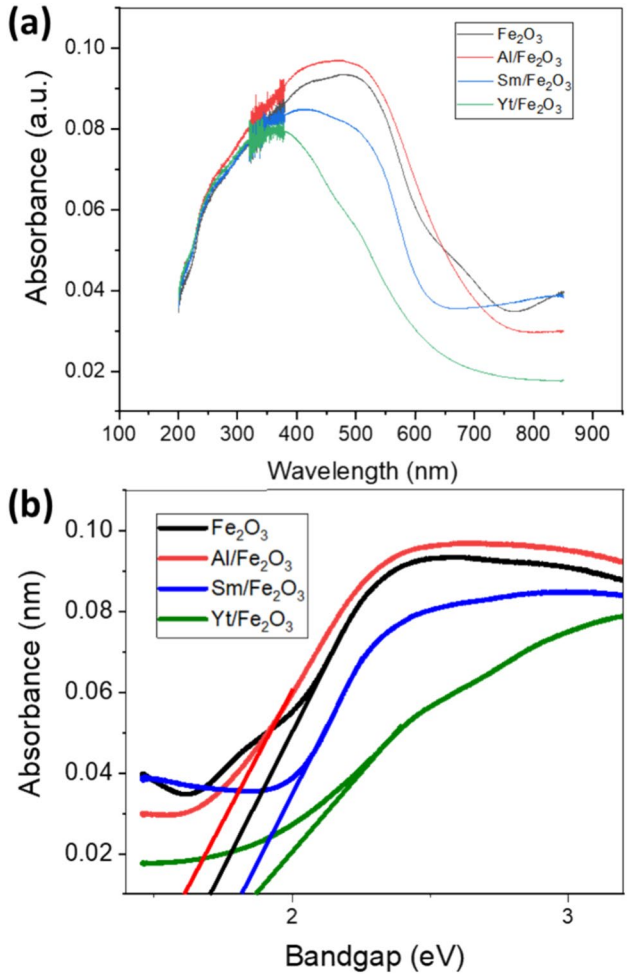

Figure 5. (**a**) UV-DRS spectra of iron oxide-based photocatalysts, (**b**) Kubelka–Munk plots with bandgap values.

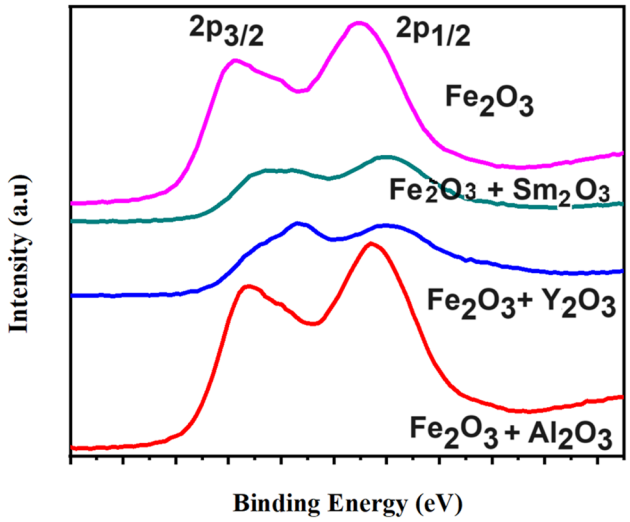

Figure 6. Valence band XPS spectra of Fe_2O_3, Al_2O_3/Fe_2O_3, Y_2O_3/Fe_2O_3 and Sm_2O_3/Fe_2O_3.

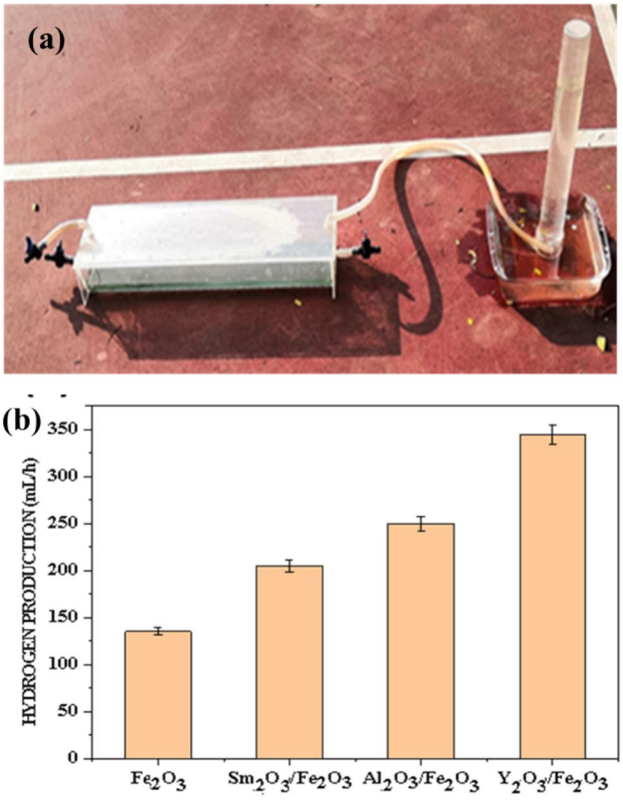

Figure 7. (**a**) Photocatalytic reactor for solar hydrogen production from sulphide wastewater, (**b**) activity of iron oxide-based photocatalysts for hydrogen production.

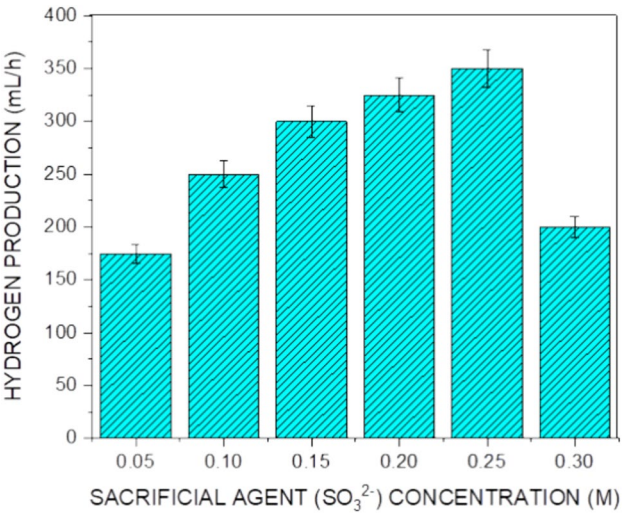

Figure 8. Effect of Sacrificial agent on photocatalytic hydrogen production.

0.25 M. A probable reason for this is that the available active sites on the surface of the photocatalyst might be competitively adsorbed by sulphite and thiosulphate thio-sulphite ions[20]. Earlier reports support the present study's findings wherein higher and lower sulphite ion concentrations against optimum concentration negatively impact the maximum H_2 production[21–23].

Effect of catalyst dose

The effect of Y_2O_3/Fe_2O_3 dose on H_2 recovery from synthetic sulphide wastewater containing 0.2 M sulphide ion concentration is determined by varying the catalyst dose from 0.05 to 0.25 g/L. Y_2O_3/Fe_2O_3 is chosen because

of its best H_2 production efficiency compared to other catalysts studied in this study. The optimal sulphite ion concentration of 0.25 M was used. The hydrogen production is recorded at regular intervals of every 1 h. Figure 9 depicts the effects of catalyst amount on hydrogen recovery. The optimal hydrogen recovery is achieved with a Y_2O_3/Fe_2O_3 dosage of 0.2 g/L. An increase in the volume of the added photocatalyst above 0.2 g/L causes the photolytic solution to become more turbid, which decreases light penetration to the Y_2O_3/Fe_2O_3 active surface and thereby reduces the rate of hydrogen recovery. Several other researchers have obtained similar findings[21,23–31].

Effect of volume of photolytic solution on H_2 production

The volume of the initial photolytic solution affects the H_2 production efficiency, as reported by earlier researchers[23–31]. Hence, the influence of 1 L to 3 L volume of reaction solution on hydrogen recovery from sulphide wastewater was analysed. The optimal sulphite ion concentrations and catalyst amount are used. Figure 10 depicts the effects of the volume of the photolytic solution on hydrogen recovery. The recovery of H_2 is found to be maximum for 1 L. On increasing the volume of the photolytic solution above 1 L, the hydrogen production decreases gradually. This shows that the light penetration is maximum at optimum volume (1 L) than increased volume (2 L, 3 L) of photolytic solution[32].

Reusability of Y_2O_3/Fe_2O_3 for H_2 recovery

For large-scale hydrogen recovery from industrial sulphide wastewater, photocatalyst stabilisation is crucial. The reuse potential of the Y_2O_3/Fe_2O_3 photocatalyst is evaluated through multiple runs to ensure its stability. To perform this recyclability test for six cycles, after each cycle, the photocatalyst from the photolytic solution was separated and washed several times with ethanol, followed by drying and grounding. Thus, the photocatalyst

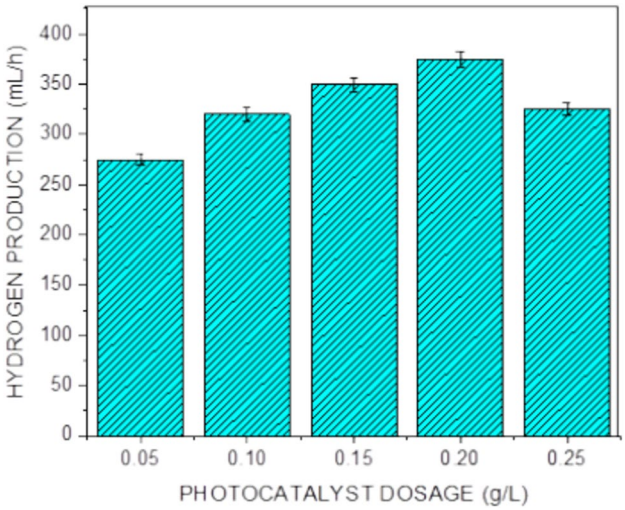

Figure 9. Effect of Y_2O_3/Fe_2O_3amount on hydrogen production.

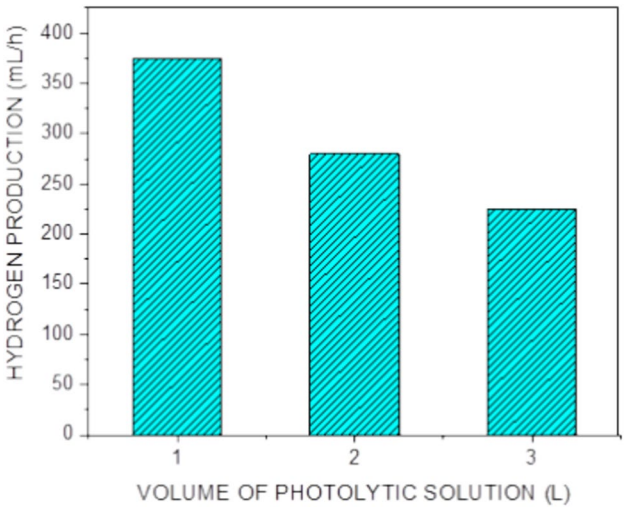

Figure 10. Effect of volume of photolytic solution.

was recycled for every cycle[33]. The reusability of Y_2O_3/Fe_2O_3 for six cycles is shown in Fig. 11. According to the results, the Y_2O_3/Fe_2O_3 is stable for up to 6 cycles.

Photocatalytic degradation of RhB dye

An inner irradiated, visible light, double-jacketed quartz photocatalytic reactor with 500 mL capacity was used to study the degradation of RhB (Fig. 12a). The photocatalytic degradation efficiencies of the as-prepared photocatalyst Fe_2O_3, Al_2O_3/Fe_2O_3, Y_2O_3/Fe_2O_3, and Sm_2O_3/Fe_2O_3 are evaluated using RhB as a model compound. With an initial concentration of 5 mg/L RhB and a photocatalyst dose of 200 mg/L, photocatalytic degradation takes place/occurs, and the results in terms of % removal of RhB are shown in Fig. 12b. RhB alone is irradiated under visible light when no catalyst is employed, and the degradation reaches 20.8% in 4 h. When the solution mixture with RhB and no catalyst is kept in a dark place, no degradation of RhB is observed. The degradation of RhB increases in the presence of photocatalysts[34–37]. The performance of pure Fe_2O_3 and Al_2O_3/Fe_2O_3 is comparable, with the highest removal efficiencies of 94% and 92%, respectively. The degradation efficiency with Fe_2O_3 and Al_2O_3/Fe_2O_3 is nearly 4.5 times that of irradiation of RhB in the absence of a photocatalyst. The removal efficiencies of Sm_2O_3/Fe_2O_3 and Y_2O_3/Fe_2O_3 are 71% and 70%, respectively, which is 3.38 times higher than without the photocatalyst. This indicates that direct photolysis of RhB results in dye degradation of up to 20%, and upon the addition of the photocatalysts, the degradation efficiency increases due to the effectiveness of the photocatalyst. RhB has an absorbance of 554.8 nm, while the photocatalysts employed in this study have a broad absorbance peak ranging from 400 to 500 nm, indicating higher light-harvesting capacity. Therefore, it is clear that the presence of photocatalysts triggers the radical-based photocatalytic dye degradation mechanism, facilitating higher removal rates of RhB.

The reuse potential of the Fe_2O_3 photocatalyst is evaluated through multiple runs to ensure its stability in the degradation of RhB dye. To perform this recyclability test for 6 cycles, after each cycle, the photocatalyst from the photolytic solution was separated and washed several times with ethanol, followed by drying and grounding. Thus, the photocatalyst was recycled for every cycle[33]. The reusability of Fe_2O_3 for 6 cycles is shown in Figure 13. According to the results, the Fe_2O_3 is stable for up to 6 cycles.

Mechanism of H_2 production and RhB degradation

Figure 14 shows the reaction mechanism for H_2 production from sulphide wastewater and RhB degradation. The band edge positions are calculated using the following formula. EVB = X − Ee + 0.5Eg and ECB = EVB − Eg. Where EVB is the potential of the valence band, ECB is the potential of the conduction band, and X is the electronegativity of the photocatalyst prepared. The Ee was the energy of free electrons on the hydrogen scale (4.5 eV), and Eg was the prepared photocatalyst's bandgap energy. In the hydrogen production study, Y_2O_3/Fe_2O_3 showed maximum yield, and the band gap of Y_2O_3/Fe_2O_3 is 1.7 eV. The E_{VB} and E_{CB} were calculated as 2.83 eV and 1.13 eV respectively. Based on the above, the mechanism of photocatalytic water splitting over Y_2O_3/Fe_2O_3 is illustrated on the right side of Fig. 14. As soon as the Y_2O_3/Fe_2O_3 is exposed to the direct irradiation in the photolytic solution containing wastewater and sacrificial agents, the electrons from the valance band (E_{VB} = 2.83 eV) jump to the conduction band (E_{CB} = 1.13 eV) leaving holes in the conduction band. Excited electrons from the valence band of the Y_2O_3/Fe_2O_3 composite material move into CB, and these photogenerated electrons and holes close the interfacial contact between Y_2O_3 and Fe_2O_3. The photogenerated electrons reduce protons to hydrogen. The photogenerated holes in the VB produce protons from wastewater.

Similarly, for RhB degradation, Fe_2O_3 shows maximum degradation efficiency. In the presence of a photocatalyst (Fe_2O_3) under irradiation, oxidation–reduction reactions enhance the degradation of RhB[31–33]. The band gap of Fe_2O_3 is 1.5 eV. The EVB and ECB were calculated as 0.47 eV and 1.03 eV respectively. Based on

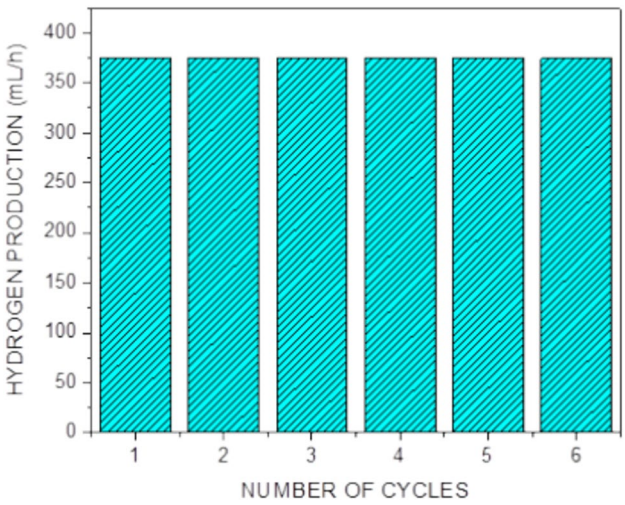

Figure 11. Reusability of Y_2O_3/Fe_2O_3.

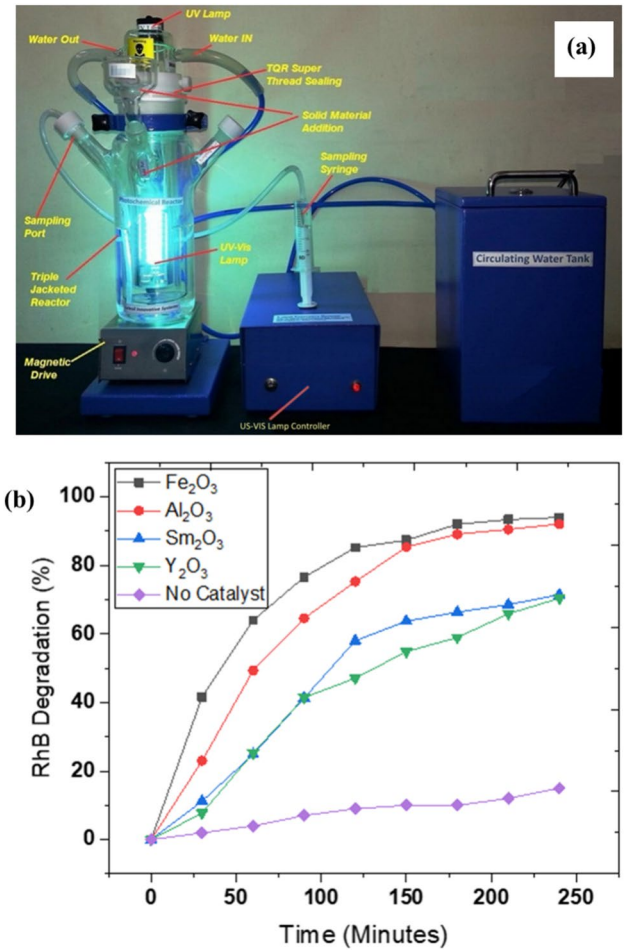

Figure 12. (**a**) Photocatalytic reactor used for RhB degradation studies, (**b**) photocatalytic degradation of RhB with various Fe_2O_3 photocatalysts (RhB = 5 mg/L; catalyst dose = 200 mg/L; initial pH range 6.5 to 8.25; temperature = 25 ± 2 °C).

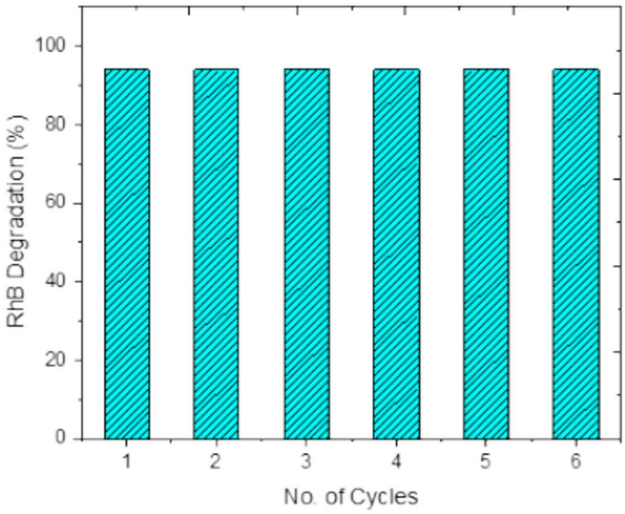

Figure 13. Reusability studies of Fe_2O_3 for RhB degradation.

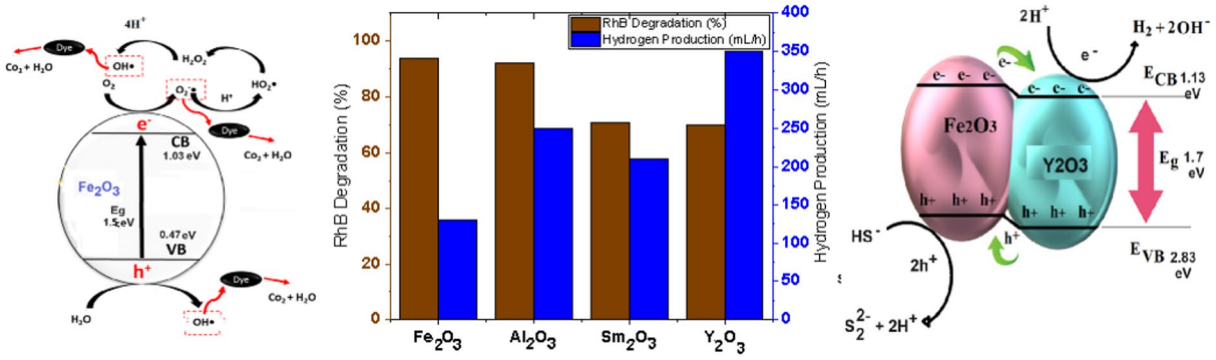

Figure 14. Mechanism of RhB degradation and H_2 production.

the above, the mechanism of RhB degradation over Fe_2O_3 is illustrated on the left side of Fig. 14. Thus, both the direct conversion of RhB and the radical-based mechanism led to the high degradation efficiency of RhB by the prepared Fe_2O_3 catalysts[38].

Conclusions

In this study, Fe_2O_3-based photocatalysts are evaluated for H_2 production from sulphide wastewater under natural sunlight. The highest H_2 production efficiency of 365 mL/h is observed using Y_2O_3/ Fe_2O_3. Y_2O_3/ Fe_2O_3 and photocatalytic reactors are effective in generating clean gas fuel (H_2) from sulphide wastewater under natural sunlight. Fe_2O_3 shows a maximum degradation efficiency of 94% of RhB. The iron oxide-based photocatalysts are noteworthy under visible light irradiation with constant pseudo-first-order kinetic rates ranging from 0.0051 to 0.0133 h^{-1}. The studied photocatalyst is noted to be stable for up to 6 consecutive cycles. In summary, iron oxide-based photocatalysts prove effective in H_2 production and dye degradation.

Data availability

The datasets used and analysed during the current study are available from the first author (Preethi Vijayarengan) on reasonable request.

Received: 16 February 2024; Accepted: 5 August 2024
Published online: 07 August 2024

References

1. Kumar, A. *et al.* High-performance photocatalytic hydrogen production and degradation of levofloxacin by wide spectrum-responsive Ag_3O_4 bridged $srTiO_3$/g-C_3N_4 plasmonic nanojunctions: Joint effect of Ag and Fe_3O_4. *ACS Appl. Mater. Interfaces* **10**, 40474–40490 (2018).
2. Kobya, M., Soltani, R. D. C., Omwene, P. I. & Khataee, A. A review on decontamination of arsenic-contained water by electrocoagulaion: Reactor configurations and operating cost along with removal mechanisms. *Environ. Technol. Innov.* **17**, 100519 (2020).
3. Muninathan, S. & Arumugam, S. Enhanced photocatalytic activities of NiS decorated reduced graphene oxide for hydrogen production and toxic dye degradation under visible light irradiation. *Int. J. Hydrogen Energy* **46**, 6532–6546 (2021).
4. Dhull, P. *et al.* An overview on ZnO-based sonophotocatalytic mitigation of aqueous phase pollutants. *Chemosphere* **333**, 138873 (2023).
5. Khan, A. A. P., Sudhaik, A., Raizada, P., Khan, A. & Rub, M. A. AgI coupled SiO_2@$CuFe_2O_4$ novel photocatalytic nano-material for photo-degradation of organic dyes. *Catal. Commun.* **179**, 106685 (2023).
6. Tahir, M. B. *et al.* Photocatalytic degradation and hydrogen evolution using bismuth tungstate-based nanocomposites under visible light irradiation. *Int. J. Hydrogen Energy* **45**, 22833–22847 (2020).
7. Zhang, F., Li, X., Zhao, Q., Chen, G. & Zhang, Q. High-performance In_2O_3@ PANI core@ shell architectures with ultra long charge carrier's lifetime for photocatalytic degradation of gaseous 1, 2-dichlorobenzene. *Appl. Catal. B Environ.* **263**, 118278 (2020).
8. Sun, J., Li, X., Zhao, Q., Tade, M. O. & Liu, S. Construction of pn heterojunction b-Bi_2O_3/$BiVO_4$ nanocomposite with improved photoinduced charge transfer property and enhanced activity in degradation of ortho-dichlorobenzene. *Appl. Catal. B Environ.* **219**, 259–268 (2017).
9. Sharma, K. *et al.* Sulphur vacancy defects engineered metal sulfides for amended photo(electro)catalytic water splitting: A review. *J. Mater. Sci. Technol.* **152**, 50–64 (2023).
10. Ismael, M. Enhanced photocatalytic hydrogen production and degradation of organic pollutants from Fe (III) doped TiO_2 nanoparticles. *J. Environ. Chem. Eng.* **8**, 103676 (2020).
11. Lakshmana, R. N., Navakoteswara, R. V., Cheralathan, K. K., Subramaniam, E. P. & Shankar, M. V. Pt/TiO_2 nanotube photocatalyst—Effect of synthesis methods on valance state of Pt and its influence on hydrogen production and dye degradation. *J. Colloid Interface Sci.* **538**, 83–98 (2019).
12. Lakshmana, R. N. *et al.* Nanostructured semiconducting materials for efficient hydrogen generation. *Environ. Chem. Lett.* **16**, 765–796 (2018).
13. Phivilay, S. P., Puretzky, A. A., Domen, K. & Wachs, I. E. Nature of catalytic active sites present on the surface of advanced bulk tantalum mixed oxide photocatalysts. *ACS Catal.* **3**, 2920–2929 (2013).
14. Kheradmand, A., Wainwright, A., Wang, L. & Jiang, Y. Anchoring iron oxides on carbon nitride nanotubes for improved photocatalytic hydrogen production. *Energy Fuels* **35**, 868–876 (2021).
15. Asif, S. A. B., Khan, S. B. & Asiri, A. Efficient solar photocatalyst based on cobalt oxide/iron oxide composite nanofibres for the detoxification of organic pollutants. *Nanoscale Res. Lett.* **9**, 510–519 (2014).
16. Shu, X., He, J. & Chen, D. Visible-light-induced photocatalyst based on nickel titanate nanoparticles. *Ind. Eng. Chem. Res.* **47**, 4750–4753 (2008).

17. Piriyawong, V., Thongpool, V., Asanithi, P. & Limsuwan, P. Preparation and characterization of alumina nanoparticles in deionized water using laser ablation technique. *J. Nanomater.* **819403**, 1–6 (2012).
18. Xiaona, Z. *et al.* Y_2O_3 modified TiO_2 nanosheets enhanced the photocatalytic removal of 4-chlorophenol and Cr (VI) in sun light. *Appl. Surf. Sci.* **410**, 134–144 (2017).
19. Ruban, P. & Sellappa, K. Development and performance of bench-scale reactor for the photocatalytic generation of hydrogen. *Energy* **73**, 926–932 (2014).
20. Grzyll, L. R., Thomas, J. J. & Barile, R. G. Photo electrochemical conversion of hydrogen sulfide to hydrogen using artificial light and solar radiation. *Int. J. Hydrogen Energy* **14**, 647–651 (1989).
21. Preethi, V. & Kanmani, S. Performance of nanophotocatalysts for the recovery of hydrogen and sulphur from sulphide containing wastewater. *Int. J. Hydrogen Energy* **43**, 3920–3934 (2018).
22. Gomathisankar, P. *et al.* Photocatalytic hydrogen production with CuS/ZnO from aqueous $Na_2S + Na_2SO_3$ solution. *Int. J. Hydrogen Energy* **38**, 8625–8630 (2013).
23. Jimmy, B. & Adesoji, A. A. The photodegradation kinetics of aqueous sodium oxalate solution using TiO_2 catalyst. *Appl. Catal. Gen.* **175**, 221–235 (1998).
24. Pareek, V. K., Chong, S., Tade, M. & Adesina, A. A. Light intensity distribution in heterogeneous photocatalytic reactors. *Asia Pac. J. Chem. Eng.* **3**, 171–201 (2008).
25. Zheng, X. J. *et al.* Research on photocatalytic H_2 production from acetic acid solution by Pt/TiO_2 nanoparticles under UV irradiation. *Int. J. Hydrogen Energy* **34**, 9033–9041 (2009).
26. Yu, L. *et al.* Simulated-sunlight-activated photocatalysis of Methylene Blue using cerium-doped SiO_2/TiO_2 nanostructured fibers. *J. Environ. Sci.* **24**, 1867–1875 (2012).
27. Dang, H., Dong, X., Dong, Y., Zhang, Y. & Hampshire, S. TiO_2 nanotubes coupled with nano-Cu $(OH)_2$ for highly efficient photocatalytic hydrogen production. *Int. J. Hydrogen Energy* **38**, 2126–2135 (2013).
28. Preethi, V. & Kanmani, S. Photocatalytic hydrogen production over $CuGa_{2-x}Fe_xO_4$ spinel. *Int. J. Hydrogen Energy* **37**, 18740–18746 (2012).
29. Priya, R. & Kanmani, S. Optimization of photocatalytic production of hydrogen from hydrogen sulfide in alkaline solution using response surface methodology. *Desalination* **276**, 222–227 (2011).
30. Estahbanati, M. R. K., Feilizadeh, M. & Iliuta, M. C. Photocatalytic valorization of glycerol to hydrogen: Optimization of operating parameters by artificial neural network. *Appl. Catal. B Environ.* **209**, 483–492 (2017).
31. Linkous, C. A., Huang, C. & Fowler, R. UV photochemical oxidation of aqueous sodium sulfide to produce hydrogen and sulphur. *J. Photochem. Photobiol. A Chem.* **168**, 153–160 (2004).
32. Preethi, V. & Kanmani, S. Performance of four various shapes of photocatalytic reactors with respect to hydrogen and sulphur recovery from sulphide containing waste streams. *J. Clean. Prod.* **133**, 1218–1226 (2016).
33. Kumar, A. *et al.* Rationally constructed synergy between dual-vacancies and Z-scheme heterostructured $MoS_{2-x}/g\text{-}C_3N_4/Ca\text{-}\alpha\text{-}Fe_2O_3$ for high-performance photodegradation of sulfamethoxazole antibiotic from aqueous solution. *Chem. Eng. J.* **474**, 145720 (2023).
34. Panchangam, S. C. *et al.* Facile fabrication of TiO_2-graphene nanocomposites (TGNCs) for the efficient photocatalytic oxidation of perfluorooctanoic acid (PFOA). *J. Environ. Chem. Eng.* **6**, 6359–6369 (2018).
35. Madjene, F., Assassi, M., Chokri, I., Enteghar, T. & Lebik, H. Optimization of photocatalytic degradation of rhodamine B using Box–Behnken experimental design: Mineralization and mechanism. *Water Environ. Res.* **93**, 112–122 (2021).
36. Lee, S. Y., Kang, D., Jeong, S., Do, H. T. & Kim, J. H. Photocatalytic degradation of Rhodamine B dye by TiO_2 and gold nanoparticles supported on a floating porous polydimethylsiloxane sponge under ultraviolet and visible light irradiation. *ACS Omega* **5**, 4233–4241 (2020).
37. Wang, Q. *et al.* Photodegradation of Rhodamine B over a novel photocatalyst of feather keratic decorated CdS under visible light irradiation. *New J. Chem.* **39**, 7112–7119 (2015).
38. Viet, P. V., Chuyen, D. V., Hien, N. Q., Duy, N. N. & Thi, M. C. Visible light induced photo-fenton degradation of rhodamine B over Fe2O3-diatomite materials. *J. Sci. Adv. Mater. Dev.* **5**, 308–315 (2020).

Author contributions

All authors contributed to the study conception and design. P.V., S.C.P, A.S., G. B. and G.K. M performed material preparation, data collection and analysis P.V. and S.C.P wrote the first draft of the manuscript All remaining authors reviewed ad edited the manuscript. All authors read and approved the final manuscript.

Competing interests

The authors declare no competing interests.

Additional information

Supplementary Information The online version contains supplementary material available at https://doi.org/10.1038/s41598-024-69413-4.

Correspondence and requests for materials should be addressed to P.V., S.C.P. or R.R.K.

Reprints and permissions information is available at www.nature.com/reprints.

Publisher's note Springer Nature remains neutral with regard to jurisdictional claims in published maps and institutional affiliations.

Open Access This article is licensed under a Creative Commons Attribution-NonCommercial-NoDerivatives 4.0 International License, which permits any non-commercial use, sharing, distribution and reproduction in any medium or format, as long as you give appropriate credit to the original author(s) and the source, provide a link to the Creative Commons licence, and indicate if you modified the licensed material. You do not have permission under this licence to share adapted material derived from this article or parts of it. The images or other third party material in this article are included in the article's Creative Commons licence, unless indicated otherwise in a credit line to the material. If material is not included in the article's Creative Commons licence and your intended use is not permitted by statutory regulation or exceeds the permitted use, you will need to obtain permission directly from the copyright holder. To view a copy of this licence, visit http://creativecommons.org/licenses/by-nc-nd/4.0/.

© The Author(s) 2024